

Effects of Laser-Annealing on Fixed-Frequency Superconducting Qubits

Hyunseong Kim,^{1,*} Christian Jünger,² Alexis Morvan,² Edward S. Barnard,³
William P. Livingston,¹ M. Virginia P. Altoé,³ Yosep Kim,² Chengyu Song,³ Larry Chen,¹
John Mark Kreikebaum,^{1,4} D. Frank Ogletree,³ David I. Santiago,^{1,2} and Irfan Siddiqi^{1,2,4}

¹*Department of Physics, University of California, Berkeley, CA 94720, USA*

²*Computational Research Division, Lawrence Berkeley National Laboratory, Berkeley, California 94720, USA*

³*Molecular Foundry Division, Lawrence Berkeley National Laboratory, Berkeley, California 94720, USA*

⁴*Materials Science Division, Lawrence Berkeley National Laboratory, Berkeley, California 94720, USA*

(Dated: June 8, 2022)

As superconducting quantum processors increase in complexity, techniques to overcome constraints on frequency crowding are needed. The recently developed method of laser-annealing provides an effective post-fabrication method to adjust the frequency of superconducting qubits. Here, we present an automated laser-annealing apparatus based on conventional microscopy components and demonstrate preservation of highly coherent transmons. In one case, we observe a two-fold increase in coherence after laser-annealing and perform noise spectroscopy on this qubit to investigate the change in defect features, in particular two-level system defects. Finally, we present a local heating model as well as demonstrate aging stability for laser-annealing on the wafer scale. Our work constitutes an important first step towards both understanding the underlying physical mechanism and scaling up laser-annealing of superconducting qubits.

INTRODUCTION

Superconducting quantum processors are a promising platform for realizing large-scale universal quantum computation [1]. In comparison to other physical platforms [2–6], superconducting quantum processors are lithographically configurable, which allows a rich variety of qubit structures and feasible scalability, currently up to ~ 100 qubits [7, 8]. Superconducting qubits require the Josephson junction (JJ), a nonlinear inductive element composed of two superconductors with a tunneling barrier in between [9, 10]. A capacitively-shunted JJ forms the transmon qubit, a widely utilized superconducting qubit with advantages ranging from high coherence to simple coupling and readout [11, 12]. As quantum processors scale up further, precise fabrication of the JJ is required to avoid qubit frequency allocation problems that can lead to frequency collisions or slow entangling gates [13–15]. However, the dispersion of state of the art JJ fabrication methods, currently $\sim 1\%$ for a 1 cm^2 chip, does not suffice the frequency constraints for a fixed-frequency multiqubit processor with even a few tens of qubits [16]. One effective technique to circumvent this problem is post-fabrication laser-annealing, in which a laser beam is applied to the JJ in order to tune the qubit frequency [17, 18]. In this work, we build upon this technique and present a laser-annealing apparatus with conventional confocal microscopy components, allowing integration into various qubit preparation processes. We demonstrate that high coherence of fixed-frequency transmon qubits is maintained after frequency shifting by laser-annealing. In one case, we observe a two-fold increase in coherence after laser-annealing. We perform noise spectroscopy to investigate this increase in coherence by comparing the change in two level system

defect features and suggest that the increase in coherence may be correlated to the decrease in spectrally neighboring TLS's after laser-annealing. Lastly, we successfully perform laser-annealing on the wafer scale with varying parameters and explain the results by using a local heating model, as well as demonstrate the stability of laser-annealing with respect to JJ aging.

LASER-ANNEALING APPARATUS AND CHARACTERIZATION

In order to facilitate integration into various qubit preparation processes, we present a laser-annealing apparatus based on confocal microscopy (schematically shown in Fig. 1(a)). A continuous, collimated laser beam (532 nm) follows the optical path depicted by the green arrows and first passes through a shutter that serves as a switch and then a neutral density filter that adjusts the beam power. The beam is then expanded and focused onto the sample stage in order to minimize the beam spot. The motorized stage automatically positions the sample on the focal plane using image detection algorithms. Imaging is performed with a CMOS camera and a white light source (not shown). This automation enables laser-annealing of both individual chips as well as 100 mm wafers with 3000 JJs.

The sample under investigation is composed of four independent transmon qubits each at different frequencies and capacitively coupled to a coplanar waveguide resonator (RO). A representative qubit-RO pair is shown in Fig. 1(b). The qubit consists of a niobium (Nb) coplanar capacitor that shunts an Al/Al-O_x/Al JJ (Fig. 1(c)). The JJs are shadow evaporated using the Manhattan style technique with typical areas of $\sim 0.1\text{ }\mu\text{m}^2$. The JJ areas

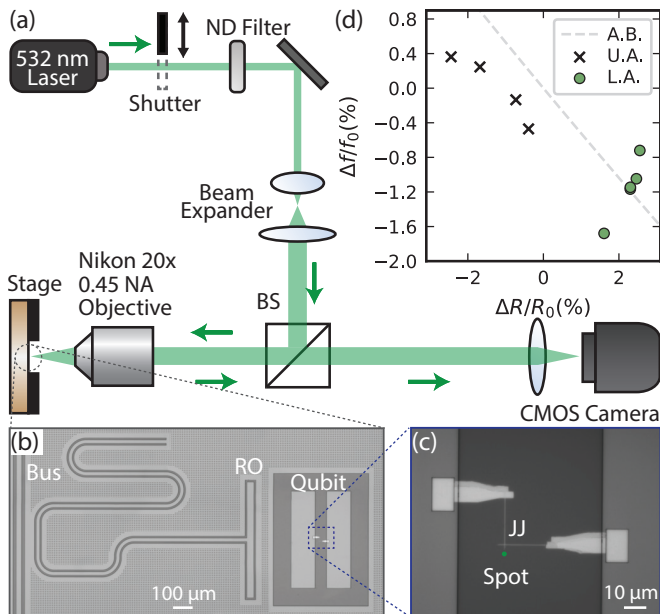


FIG. 1. (a) Schematic of laser-annealing apparatus. The continuous wave, 532 nm, 40 mW diode-pumped solid state laser beam follows the optical path shown by the green arrows and is focused down to a beam waist of 0.81 μm . Abbreviated optical components are labeled as follows: Neutral Density (ND) filter, Beam Splitter (BS), and Numerical Aperture (NA). (b) Optical image of fixed-frequency transmon qubit, consisting of Al/Al-O_x/Al Josephson junction (JJ), shunted by niobium (Nb) planar capacitor. The qubit is capacitively coupled to a Nb quarter-wavelength coplanar waveguide resonator (RO) and read out through the bus. (c) Optical magnification of JJ. Laser spot depicted by green circle and drawn to scale. (d) Predicted (gray dashed line derived from Ambegaokar-Baratoff (A.B.) formula) and measured qubit frequency shift ($\Delta f/f_0$) with respect to change in room temperature resistance ($\Delta R/R_0$) due to laser-annealing (L.A.). Unannealed samples are labeled U.A.

are varied to differ the frequencies of the four qubits. To isolate the effects of laser-annealing, we minimize resonator-induced decay and drive the qubit through the readout bus (RO) [7]. Further details regarding the setup and fabrication are given in the Supplemental Materials (S.M.).

We apply laser-annealing to the JJ's of five transmon qubits and investigate the response in normal state resistance R_N at room temperature and the resulting shift in qubit frequency f_Q at ~ 20 mK. We measure R_N using a lock-in voltage probe with the probing needles electrically contacting the Nb capacitors. From R_N , we utilize the Ambegaokar-Baratoff formula to calculate the critical current I_C , nominally around 35 nA [19]. Applying the transmon-regime approximation with I_C , the predicted qubit frequency in the superconducting state is given by:

$$hf_Q = \sqrt{(h\Delta_{\text{Al}}E_C)/(e^2R_N) - E_C} \quad (1)$$

where h is Planck's constant, e the electron charge, Δ_{Al} the Al superconducting gap ($=170 \mu\text{eV}$), and E_C the charging energy of the transmon ($E_C/h \sim 275$ MHz) [7]. We expect laser-annealing to increase R_N and resultantly shift down f_Q , while Δ_{Al} and E_C remain constant.

The normalized change in qubit frequency ($\Delta f/f_0$) is plotted as a function of change in normal state resistance ($\Delta R/R_0$) in Fig. 1(d), where f_0 and R_0 are the initial frequency and resistance. The prediction (gray dashed line) is given by: $\Delta f_Q^P/f_{Q,0}^P = -(1/1.9)\Delta R/R_0$. This is derived from Eq. 1 using $\Delta R/R_0 \ll 1$ and applying a 5% correction to the slope due to E_C . Both unannealed (black cross) and laser-annealed (green circles) qubits follow the trend of the prediction, with a controlled frequency downshift for the laser-annealed qubits. The frequency shift of the four unannealed qubits, due to air reexposure during the laser-annealing step and frequency fluctuations across cryostat cooldowns, average to zero with a variation of $\pm 0.3\%$ [20]. The resistance drift of the unannealed qubits as well as the discrepancies between prediction and measurement may be due to differences between the expected and actual values of Δ_{Al} and E_C , as well as electrical contact variations across multiple resistance probings.

HIGH COHERENCE AND TWO-LEVEL SYSTEM SPECTROSCOPY

We have so far demonstrated tunability of qubit frequency using laser-annealing. We now evaluate the quality of laser-annealed qubits. In particular, the qubit relaxation (T_1) and phase coherence (T_2) times are measured since these metrics are highly sensitive to degradation in materials quality [21]. To study the statistical features, we acquire the T_1 and T_2 of the transmons for ~ 17 hours before and after laser-annealing. The T_1 acquisitions are shown in Fig. 2(a). Apart from Q5, the coherence medians of laser-annealed qubits Q1_L-Q4_L (stars in green boxes) lie within three standard deviations of the medians of Q1-Q4 (caps of white boxes), indicating no statistically significant differences. Similarly, the T_2 coherence times do not exhibit any statistically significant differences after laser-annealing (see Fig. 2(b)). On average, the T_1 of Q1_L-Q4_L meet the current standards for high coherence times of $\sim 100 \mu\text{s}$ [22]. These results verify that our setup successfully performs controlled frequency shifts while preserving high qubit coherence.

In the case of Q5, we observe a statistically significant increase in both T_1 (46.5 μs to 95.0 μs) and T_2 (29.0 μs to 49.8 μs) coherence after laser-annealing. In contrast to Q1-Q4, Q5 has an additional CPW to drive the qubit, enabling noise spectroscopy that can help investigate the increase in coherence. Several different noise sources can hinder coherence, such as dielectric loss, quasi-particle tunneling, and cosmic radiation [22–24].

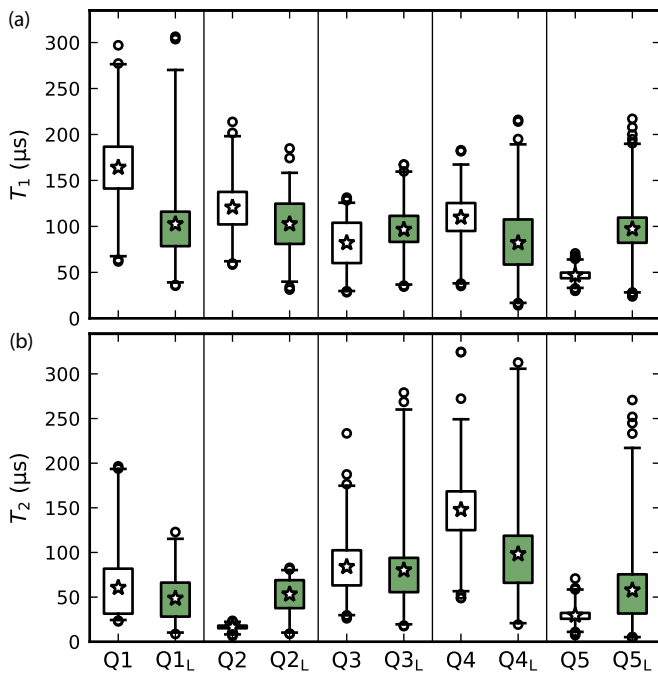


FIG. 2. Comparison of (a) T_1 and (b) T_2 coherence times of four qubits before (Q1-Q5) and after laser-annealing (Q1L-Q5L). Each boxplot consists of the mean (star), interquartile range (box boundaries), three standard deviation range (caps), and outliers (white circles) of the 17 hour acquisitions of each qubit. The T_2 measurements of Q2 yielded poor results and large fitting errors, leading to low statistics. Q5 exhibits a two-fold increase in coherence and is used for TLS spectroscopy.

In particular, losses due to dielectrics at the metal-air, metal-substrate, and substrate-air interfaces of superconducting qubits can transversely couple and potentially induce energy relaxations [21]. These dielectric losses can be modeled as two-level systems (TLS) with transition frequencies f_{TLS} and coupling g to the qubit. The qubit relaxation rate $\Gamma_1 = 1/T_1$ increases the closer f_Q is to f_{TLS} . In particular, Γ_1 follows a Lorentzian profile with respect to qubit-TLS detuning $\Delta = f_Q - f_{\text{TLS}}$: $\Gamma_1 = (2\Gamma g^2)/(\Gamma^2 + \Delta^2) + \Gamma_{1,Q}$ where Γ is the sum of TLS and qubit energy relaxation and dephasing rates and $\Gamma_{1,Q}$ the frequency-independent qubit energy relaxation rate [21, 25]. Hence a spectral and temporal sweep of qubit T_1 , or TLS spectroscopy, can probe the noise environment of a transmon qubit [26–28]. We perform TLS spectroscopy on Q5 before and after laser-annealing in order to detect changes in TLS features. We do so by AC Stark shifting the qubit using an off-resonant tone of frequency $f_Q \pm 80$ MHz [27]. The frequency shift is proportional to the square of the tone amplitude, hence the drive CPW is required to deliver higher power in comparison to driving through the RO [29]. With this configuration, we are able to reliably shift f_Q by ± 33 MHz, measured by a Ramsey sequence. For fast acquisition, we measure the

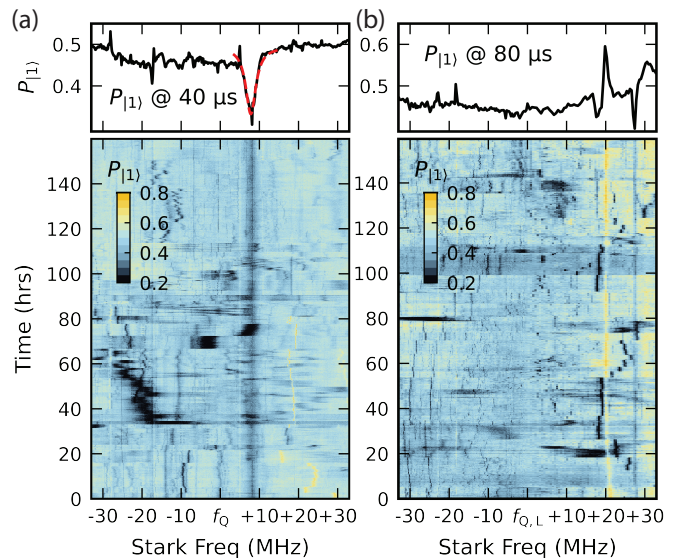


FIG. 3. (a) Spectral and temporal profile of Q5. Colorbar is scale for excited state population $P_{|1\rangle}$. Here, $P_{|1\rangle}$ is measured at 40 μs . Time-averaged spectral profile is shown on top with fit using Lorentzian around the constant TLS. From the fit, $f_{\text{TLS}} = f_Q + 7.81$ MHz. (b) Spectral and temporal profile of laser-annealed qubit (Q5L). Here, $P_{|1\rangle}$ is measured at 80 μs . $f_{Q,L} = f_Q - 94$ MHz. Time-averaged spectral profile on top. No persistent defects are visible.

average excited state population $P_{|1\rangle}$ around T_1 .

TLS spectroscopy of 160 hours is shown both before (Fig. 3(a)) and after (Fig. 3(b)) laser-annealing. In Fig. 3(a), one consistent and several fluctuating (dark areas) TLS features are observed close to the initial qubit frequency f_Q . Fitting to the Lorentzian, we find the consistent TLS is coupled to the qubit with $g = 76$ kHz and lies 7.81 MHz away from f_Q , which is more than three linewidths away from f_{TLS} . The low coupling and large spectral distance make it unlikely for this single TLS to solely limit the qubit coherence. If the dominant decoherence channel originates from TLS, it may be due to multiple TLS's that are weakly coupled to the qubit over a wide frequency range around f_Q . In contrast, we observe reduced TLS features in the spectral vicinity of the qubit in Fig. 3(b) after f_Q is downshifted by 94 MHz. We repeat TLS spectroscopy for two more cooldowns to evaluate the spectral features of the qubit due to thermal cycling, and do not observe significant differences with respect to Fig. 3 (see Fig. S1) [30, 31]. We suggest that the increase in coherence may be correlated to the decrease in spectrally neighboring TLS's after laser-annealing. Additional studies with a wider spectral range are needed to investigate this. However, our observation opens possibilities to healing a defective qubit on a multiqubit processor using laser-annealing and TLS spectroscopy under the condition that the TLS features are consistent across cooldowns.

LASER-ANNEALING MECHANISM

In this section we investigate the response of R_N to lasing parameters at the wafer-scale in order to understand the laser-annealing mechanism. This is enabled by the automated JJ image recognition of our setup, which positions and focuses the JJ with respect to the beam within 20 s [32]. We utilize JJ test wafers with 3000 junctions similar to Ref. [16]. Across multiple wafers, we study four lasing parameters: power, spot displacement from the JJ, exposure time, and exposure repetition, as well as stability to aging (see Fig. 4, Fig. S2, and Table. 1). Table. S1 in the S.M. provides all parameters of each study.

Based on previous studies of JJ thermal annealing, we hypothesize that laser-annealing locally heats the JJ and thickens the tunneling barrier, thereby increasing R_N [33–35]. We first verify local heating by measuring the normalized resistance change ($\Delta R/R_0$) of JJs with three different areas with respect to lasing power (Fig. 4(a)). The normalized resistance change follows an exponentially plateauing function (red dashed line) that caps at $\Delta R/R_0 = 1.8\%$. This trend is similar to that of low temperature ($< 150^\circ\text{C}$) thermal annealing of JJs demonstrated by [33, 36–38]. In order to correlate JJ temperature to laser power, we simulate the temperature (T) of a JJ directly illuminated by a Gaussian beam with waist $0.81\ \mu\text{m}$ of varying power (P) using COMSOL Multiphysics. We observe a linear increase $T(P) = 2.47P + 20^\circ\text{C}$ that reaches $\sim 120^\circ\text{C}$ at $P = 40\ \text{mW}$. The resistance change at this temperature is similar to $\Delta R/R_0$ observed in the literature [36, 37]. Extending the comparison with thermal annealing, for lasing powers $> 50\ \text{mW}$ for our setup, which corresponds to JJ temperatures $> 150^\circ\text{C}$ as given by $T(P)$, we expect a rapid increase in R_N . This is because in this temperature regime, accelerated growth of R_N has been observed [36–38].

Next we investigate the heat absorption mechanism by studying the normalized resistance change with respect to laser spot displacement (D) from the JJ. The displacement is measured from below the junction center, as shown in the inset of Fig. 4(b). We observe that the measured $\Delta R/R_0$ (blue points) is maximized at a displacement of $4\ \mu\text{m}$, which corresponds to the extension length of the Al electrodes beneath the JJs. This is due to two competing effects: increased reflection from Al/Al-O_x as displacement is reduced and decreased heat transfer from the Si substrate as displacement is increased. We model the power loss from reflection by calculating the absorbed power with respect to beam displacement using Gaussian beam integration. We then multiply this absorption function with an exponentially decaying function ($H(D) = A \exp(-D/D_0) + B$) that models heat transfer, where D_0 is the characteristic decay length for thermal conduction (see Fig. S2) [39, 40]. We use this

product function to fit the data (red dashed line). The reflection is minimized at $D > 4\ \mu\text{m}$ and $D_0 = 9.5\ \mu\text{m}$, resulting in a maximum fitted $\Delta R/R_0$ at $D = 5\ \mu\text{m}$. The kink at $D = 4\ \mu\text{m}$ is due to the increased absorption as the spot moves away from the Al electrode and onto the Si. It can also be seen that when the beam is placed more than $30\ \mu\text{m}$ away from the JJ, the change in resistance approaches that of unannealed JJs (gray dashed line). In other words, R_N is unaffected by a beam displaced more than $30\ \mu\text{m}$. This demonstrates locality of the laser heating on the sub-millimeter length scale.

Based on the measurements, we suggest that the laser beam locally heats the JJs through the Si substrate. Heat absorption has been proposed to thicken the JJ tunnel barrier in studies based on thermal annealing [33]. Therefore, we measure the barrier thickness using high resolution transmission electron microscopy and fit the area-normalized R_N to the exponential of barrier thickness (see Fig. S3 and Table. S2) [41]. From the fit, we estimate that a 30% change in R_N can originate from a $\sim \text{\AA}$ change in tunnel barrier thickness. However, due to the non-uniformity of the barrier (dispersion $\sim 0.4\ \text{nm}$), we are unable to detect the corresponding increase in thickness ($0.04\ \text{nm}$) of a $< 10\%$ change in R_N caused by laser-annealing. This non-uniformity makes it unlikely for a simple barrier thickening model to fully explain the microscopic mechanism. Instead, consideration of other microscopic factors, such as barrier height and chemical composition changes at the Al/Al-O_x interface, is needed [35].

Lastly, we study how robust laser-annealing is with respect to aging. JJ aging refers to the increase in R_N with exposure to air in time [33, 42]. While the drift in R_N due to aging is currently unavoidable, it is important that the resistance difference between laser-annealed and unannealed JJs is conserved for an extended period of time. For superconducting qubits, this translates to maintaining frequency differences between different qubits, which is important for frequency allocation. We study the robustness against aging as follows. We prepare two wafers, one with newly fabricated JJs (Wafer1) and the other with 130 day aged JJs (Wafer2). Wafer2 serves to show the drift in R_N when aging effects are minimal. For each wafer, we probe the resistance of unannealed and laser-annealed JJs for a period of 30 days, stored in atmosphere. All four data groups are fit to an exponentially plateauing aging function, with the fit parameters given in Table. 1 [16]. As can be seen in Fig. 4(c), aging effects are pronounced for Wafer1 (16%) in comparison to Wafer2 (7%). Furthermore, the standard deviation increases with respect to time, implying varying degrees of aging even amongst nominally identical JJs. However, on average, the difference in resistance change between unannealed and laser-annealed JJs for each wafer is maintained even after 30 days of aging. This demonstrates that laser-annealing is robust against aging. The

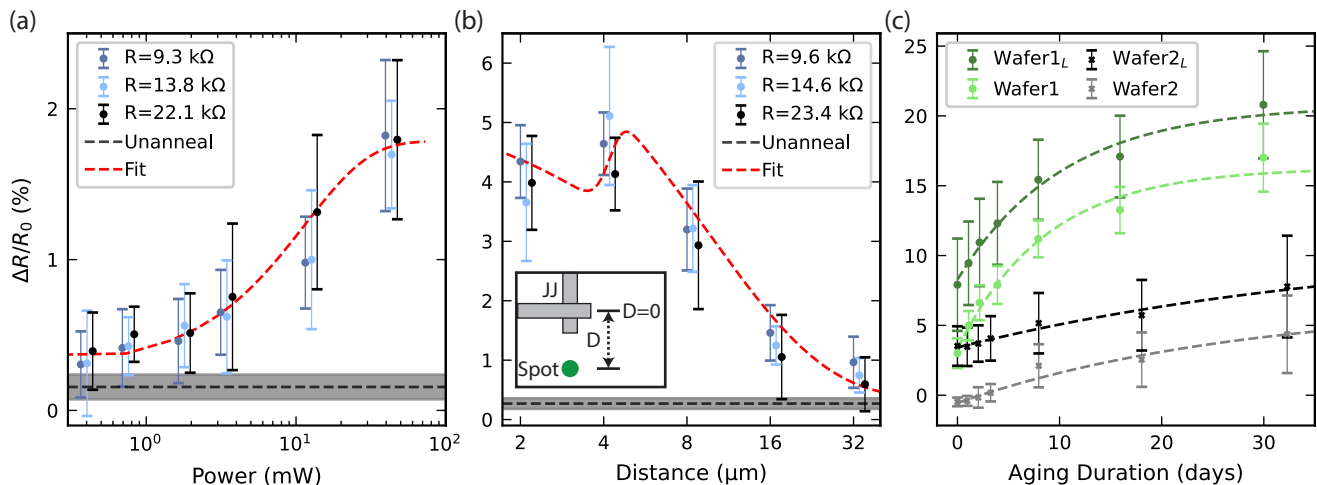


FIG. 4. Wafer scale characterization of laser-annealing. Different wafers are utilized for each subfigure. (a) Percent JJ resistance change vs laser power. Fit using exponential plateau function of simulated temperature at junction. Each point is the average of ~ 20 JJs, with the standard deviation given by the errorbars. Unannealed JJs shown by the gray dashed line, with standard deviation shown by the gray shaded region. (b) Percent JJ resistance change vs laser spot displacement from JJ. Maximum resistance change when the spot is displaced $4\mu\text{m}$ from the junction. Fit using product of heat transfer and absorbed power. (Inset) Schematic of experiment. Distance (D) is measured from below the center of the JJ. (c) Stability of laser-annealing with respect to JJ aging in atmosphere. Each dashed line is data fit to exponentially plateauing function. Wafers 1 and 2 each correspond to new and aged junction wafers, with annealed junctions labeled by subscript L. Day 0 corresponds to the day of laser-annealing.

wafer-scale study we have conducted in this section constitutes a first step in both wafer-scale applicability of laser-annealing, as well as investigating the underlying physical mechanism.

Sample	Final Resistance Change	Initial Resistance Change	Aging Constant
Wafer1 _L	$21 \pm 1.2\%$	$9 \pm 1.7\%$	10.40 ± 2.5 days
Wafer1	$16 \pm 1.1\%$	$3 \pm 1.6\%$	8.72 ± 1.7 days
Wafer2 _L	$11 \pm 5.4\%$	$3 \pm 7.6\%$	41.15 ± 39.4 days
Wafer2	$7 \pm 4.0\%$	$0 \pm 5.6\%$	27.95 ± 21.5 days

TABLE 1. Fit parameters for Fig. 4(c). The fit is done using an exponential plateau function $\Delta R/R_0 = A - B \exp(-t/\tau)$, where A corresponds to the Final Resistance Change, $(A-B)$ the Initial Resistance Change, and τ the Aging Constant. The large fitting errors for Wafer2 are due to fitting an exponential at the tail.

CONCLUSION

We have constructed an automated laser-annealing apparatus using conventional microscopy components and demonstrated reliable frequency tuning of fixed-frequency transmon qubits. The high coherence of our transmons is preserved after laser-annealing. We have further observed an instance of coherence increase after laser-annealing, and performed TLS spectroscopy to

investigate the change in defect features. These methods should be further explored towards treating defective qubits on multiqubit quantum processors.

Furthermore, we have scaled up laser-annealing and studied effects of lasing parameters at the wafer scale. With this, we have put forth a model of local heating through the Si substrate. Additional studies with a change or etching of substrate underneath the JJ can help verify this model [43–45]. We have also demonstrated that laser-annealing is robust against aging, which is important for superconducting qubits since the time between laser-annealing and qubit measurement is non-negligible. Further studies are needed to correlate normalized R_N to JJ barrier thickness. This can be realized using different JJ geometries or different JJ materials. Efforts in this direction are necessary since a thorough understanding of each fabrication and treatment step is ultimately required as qubit coherence times are pushed higher into the millisecond regime.

ACKNOWLEDGMENTS

The authors thank B. Marinelli for useful discussions regarding TLS. This work was funded by the U.S. Department of Energy, Office of Science, Office of Basic Energy Sciences, Materials Sciences and Engineering Division under Contract No. DE-AC02-05-CH11231 “High-Coherence Multilayer Superconducting Structures for Large Scale Qubit Integration and Photonic Transduc-

tion program (QIS-LBNL)⁷. Comsol simulations were performed in the Molecular Graphics and Computation Facility at UC Berkeley, which is funded by the Kavli Institute and NIH S10OD023532. Focused ion beaming (FIB) for HRTEM was conducted at the Surface Analysis Lab at University of Utah by Brian Van Devenner and Randy C. Polson.

* Email: hyunkim@berkeley.edu

- [1] F. Arute, K. Arya, R. Babbush, D. Bacon, J. C. Bardin, R. Barends, R. Biswas, S. Boixo, F. G. S. L. Brandao, D. A. Buell, B. Burkett, Y. Chen, Z. Chen, B. Chiaro, R. Collins, W. Courtney, A. Dunsworth, E. Farhi, B. Foxen, A. Fowler, C. Gidney, M. Giustina, R. Graff, K. Guerin, S. Habegger, M. P. Harrigan, M. J. Hartmann, A. Ho, M. Hoffmann, T. Huang, T. S. Humble, S. V. Isakov, E. Jeffrey, Z. Jiang, D. Kafri, K. Kechedzhi, J. Kelly, P. V. Klimov, S. Knysh, A. Korotkov, F. Kostritsa, D. Landhuis, M. Lindmark, E. Lucero, D. Lyakh, S. Mandrà, J. R. McClean, M. McEwen, A. Megrant, X. Mi, K. Michielsen, M. Mohseni, J. Mutus, O. Naaman, M. Neeley, C. Neill, M. Y. Niu, E. Ostby, A. Petukhov, J. C. Platt, C. Quintana, E. G. Rieffel, P. Roushan, N. C. Rubin, D. Sank, K. J. Satzinger, V. Smelyanskiy, K. J. Sung, M. D. Trevithick, A. Vainsencher, B. Villalonga, T. White, Z. J. Yao, P. Yeh, A. Zalcman, H. Neven, and J. M. Martinis, Quantum supremacy using a programmable superconducting processor, *Nature* **574**, 505 (2019).
- [2] J. I. Cirac and P. Zoller, Quantum computations with cold trapped ions, *Physical Review Letters* **74**, 4091 (1995).
- [3] D. Loss and D. P. DiVincenzo, Quantum computation with quantum dots, *Physical Review A* **57**, 120 (1998).
- [4] A. Imamoglu, D. D. Awschalom, G. Burkard, D. P. DiVincenzo, D. Loss, M. Sherwin, and A. Small, Quantum information processing using quantum dot spins and cavity QED, *Physical Review Letters* **83**, 4204 (1999).
- [5] R. Hanson, O. Gywat, and D. D. Awschalom, Room-temperature manipulation and decoherence of a single spin in diamond, *Physical Review B* **74**, 161203 (2006).
- [6] E. Knill, R. Laflamme, and G. J. Milburn, A scheme for efficient quantum computation with linear optics, *Nature* **409**, 46 (2001).
- [7] P. Krantz, M. Kjaergaard, F. Yan, T. P. Orlando, S. Gustavsson, and W. D. Oliver, A quantum engineer's guide to superconducting qubits, *Applied Physics Reviews* **6**, 021318 (2019).
- [8] P. Ball, First quantum computer to pack 100 qubits enters crowded race, *Nature* **599**, 542 (2021).
- [9] B. Josephson, Possible new effects in superconductive tunnelling, *Physics Letters* **1**, 251 (1962).
- [10] B. D. Josephson, Coupled superconductors, *Reviews of Modern Physics* **36**, 216 (1964).
- [11] J. Koch, T. M. Yu, J. Gambetta, A. A. Houck, D. I. Schuster, J. Majer, A. Blais, M. H. Devoret, S. M. Girvin, and R. J. Schoelkopf, Charge-insensitive qubit design derived from the cooper pair box, *Physical Review A* **76**, 042319 (2007).
- [12] C. Wang, X. Li, H. Xu, Z. Li, J. Wang, Z. Yang, Z. Mi, X. Liang, T. Su, C. Yang, G. Wang, W. Wang, Y. Li, M. Chen, C. Li, K. Linghu, J. Han, Y. Zhang, Y. Feng, Y. Song, T. Ma, J. Zhang, R. Wang, P. Zhao, W. Liu, G. Xue, Y. Jin, and H. Yu, Towards practical quantum computers: transmon qubit with a lifetime approaching 0.5 milliseconds, *npj Quantum Information* **8**, 3 (2022).
- [13] A. Morvan, L. Chen, J. M. Larson, D. I. Santiago, and I. Siddiqi, Optimizing frequency allocation for fixed-frequency superconducting quantum processors, [arXiv:2112.01634](https://arxiv.org/abs/2112.01634) (2021).
- [14] M. Brink, J. M. Chow, J. Hertzberg, E. Magesan, and S. Rosenblatt, Device challenges for near term superconducting quantum processors: frequency collisions, in *2018 IEEE International Electron Devices Meeting (IEDM)* (IEEE, 2018).
- [15] L. B. Nguyen, G. Koolstra, Y. Kim, A. Morvan, T. Chistolini, S. Singh, K. N. Nesterov, C. Jünger, L. Chen, Z. Pedramrazi, B. K. Mitchell, J. M. Kreikebaum, S. Puri, D. I. Santiago, and I. Siddiqi, Scalable high-performance fluxonium quantum processor, [arXiv:2201.09374](https://arxiv.org/abs/2201.09374) (2022).
- [16] J. M. Kreikebaum, K. P. O'Brien, A. Morvan, and I. Siddiqi, Improving wafer-scale josephson junction resistance variation in superconducting quantum coherent circuits, *Superconductor Science and Technology* **33**, 06LT02 (2020).
- [17] J. B. Hertzberg, E. J. Zhang, S. Rosenblatt, E. Magesan, J. A. Smolin, J.-B. Yau, V. P. Adiga, M. Sandberg, M. Brink, J. M. Chow, and J. S. Orcutt, Laser-annealing josephson junctions for yielding scaled-up superconducting quantum processors, *npj Quantum Information* **7**, 129 (2021).
- [18] E. J. Zhang, S. Srinivasan, N. Sundaresan, D. F. Bogorin, Y. Martin, J. B. Hertzberg, J. Timmerwilke, E. J. Pritchett, J.-B. Yau, C. Wang, W. Landers, E. P. Lewandowski, A. Narasgond, S. Rosenblatt, G. A. Keefe, I. Lauer, M. B. Rothwell, D. T. McClure, O. E. Dial, J. S. Orcutt, M. Brink, and J. M. Chow, High-performance superconducting quantum processors via laser annealing of transmon qubits, *Science Advances* **8**, 19 (2022).
- [19] V. Ambegaokar and A. Baratoff, Tunneling between superconductors, *Physical Review Letters* **10**, 486 (1963).
- [20] C. R. H. McRae, G. M. Stiehl, H. Wang, S.-X. Lin, S. A. Caldwell, D. P. Pappas, J. Mutus, and J. Combes, Reproducible coherence characterization of superconducting quantum devices, *Applied Physics Letters* **119**, 100501 (2021).
- [21] J. Lisenfeld, A. Bilmes, A. Megrant, R. Barends, J. Kelly, P. Klimov, G. Weiss, J. M. Martinis, and A. V. Ustinov, Electric field spectroscopy of material defects in transmon qubits, *npj Quantum Information* **5**, 105 (2019).
- [22] I. Siddiqi, Engineering high-coherence superconducting qubits, *Nature Reviews Materials* **6**, 875 (2021).
- [23] C. Wang, Y. Y. Gao, I. M. Pop, U. Vool, C. Axline, T. Brecht, R. W. Heeres, L. Frunzio, M. H. Devoret, G. Catelani, L. I. Glazman, and R. J. Schoelkopf, Measurement and control of quasiparticle dynamics in a superconducting qubit, *Nature Communications* **5**, 5836 (2014).
- [24] A. P. Vepsäläinen, A. H. Karamlou, J. L. Orrell, A. S. Dogra, B. Loer, F. Vasconcelos, D. K. Kim, A. J. Melville, B. M. Niedzielski, J. L. Yoder, S. Gustavsson, J. A. Formaggio, B. A. VanDevender, and W. D. Oliver, Impact

- of ionizing radiation on superconducting qubit coherence, *Nature* **584**, 551 (2020).
- [25] R. Barends, J. Kelly, A. Megrant, D. Sank, E. Jeffrey, Y. Chen, Y. Yin, B. Chiaro, J. Mutus, C. Neill, P. O'Malley, P. Roushan, J. Wenner, T. C. White, A. N. Cleland, and J. M. Martinis, Coherent josephson qubit suitable for scalable quantum integrated circuits, *Physical Review Letters* **111**, 080502 (2013).
- [26] P. Klimov, J. Kelly, Z. Chen, M. Neeley, A. Megrant, B. Burkett, R. Barends, K. Arya, B. Chiaro, Y. Chen, A. Dunsworth, A. Fowler, B. Foxen, C. Gidney, M. Giustina, R. Graff, T. Huang, E. Jeffrey, E. Lucero, J. Mutus, O. Naaman, C. Neill, C. Quintana, P. Roushan, D. Sank, A. Vainsencher, J. Wenner, T. White, S. Boixo, R. Babbush, V. Smelyanskiy, H. Neven, and J. Martinis, Fluctuations of energy-relaxation times in superconducting qubits, *Physical Review Letters* **121**, 090502 (2018).
- [27] M. Carroll, S. Rosenblatt, P. Jurcevic, I. Lauer, and A. Kandala, Dynamics of superconducting qubit relaxation times, [arXiv:2105.15201](https://arxiv.org/abs/2105.15201) (2021).
- [28] J. H. Béjanin, C. T. Earnest, A. S. Sharafeldin, and M. Mariantoni, Interacting defects generate stochastic fluctuations in superconducting qubits, *Physical Review B* **104**, 094106 (2021).
- [29] A. Schneider, J. Braumüller, L. Guo, P. Stehle, H. Rotzinger, M. Marthaler, A. V. Ustinov, and M. Weides, Local sensing with the multilevel ac stark effect, *Physical Review A* **97**, 062334 (2018).
- [30] J. J. Burnett, A. Bengtsson, M. Scigliuzzo, D. Niepce, M. Kudra, P. Delsing, and J. Bylander, Decoherence benchmarking of superconducting qubits, *npj Quantum Information* **5**, 54 (2019).
- [31] S. E. de Graaf, L. Faoro, L. B. Ioffe, S. Mahashabde, J. J. Burnett, T. Lindström, S. E. Kubatkin, A. V. Danilov, and A. Y. Tzalenchuk, Two-level systems in superconducting quantum devices due to trapped quasiparticles, *Science Advances* **6**, 51 (2020).
- [32] D. B. Durham, D. F. Ogletree, and E. S. Barnard, Scanning auger spectromicroscopy using the scopefoundry software platform, *Surface and Interface Analysis* **50**, 1174 (2018).
- [33] P. J. Koppinen, L. M. Väistö, and I. J. Maasilta, Complete stabilization and improvement of the characteristics of tunnel junctions by thermal annealing, *Applied Physics Letters* **90**, 053503 (2007).
- [34] C. Granata, L. Petti, M. Rippa, S. Rombetto, B. Ruggiero, M. Russo, R. Russo, and A. Vettoliere, Spatial modulation of critical current density in niobium based josephson junctions induced by selective heating, *Applied Physics Letters* **102**, 222603 (2013).
- [35] C. Granata, A. Vettoliere, L. Petti, M. Rippa, B. Ruggiero, P. Mormile, and M. Russo, Localized laser trimming of critical current in niobium based josephson devices, *Applied Physics Letters* **90**, 232503 (2007).
- [36] J. Migacz and M. Huber, Thermal annealing of nb/al-AIO/sub x//nb josephson junctions, *IEEE Transactions on Applied Superconductivity* **13**, 123 (2003).
- [37] T. Shiota, T. Imamura, and S. Hasuo, Fabrication of high quality nb/AIO/sub /x-al/nb josephson junctions. III. annealing stability of AIO/sub /x tunneling barriers, *IEEE Transactions on Applied Superconductivity* **2**, 222 (1992).
- [38] A. Vettoliere, O. Talamo, P. Silvestrini, M. Valentino, and C. Granata, Fine optimization of josephson critical current in SQUID devices by thermal annealing, *Journal of Physics: Conference Series* **1559**, 012014 (2020).
- [39] M. A. Green and M. J. Keevers, Optical properties of intrinsic silicon at 300 k, *Progress in Photovoltaics: Research and Applications* **3**, 189 (1995).
- [40] Z.-Y. Wang, R.-J. Zhang, H.-L. Lu, X. Chen, Y. Sun, Y. Zhang, Y.-F. Wei, J.-P. Xu, S.-Y. Wang, Y.-X. Zheng, and L.-Y. Chen, The impact of thickness and thermal annealing on refractive index for aluminum oxide thin films deposited by atomic layer deposition, *Nanoscale Research Letters* **10**, 46 (2015).
- [41] A. Kleinsasser, R. Miller, and W. Mallison, Dependence of critical current density on oxygen exposure in nb-AIO/sub x/-nb tunnel junctions, *IEEE Transactions on Applied Superconductivity* **5**, 26 (1995).
- [42] J. Schafer and C. J. Adkins, Annealing effects and oxide structure in alumina tunnelling barriers, *Journal of Physics: Condensed Matter* **3**, 2907 (1991).
- [43] Z. Degnan, X. He, A. G. Frieiro, Y. P. Sachkou, A. Fedorov, and P. Jacobson, Ternary metal oxide substrates for superconducting circuits, [arXiv:2201.06228](https://arxiv.org/abs/2201.06228) (2022).
- [44] Y. Chu, C. Axline, C. Wang, T. Brecht, Y. Y. Gao, L. Frunzio, and R. J. Schoelkopf, Suspending superconducting qubits by silicon micromachining, *Applied Physics Letters* **109**, 112601 (2016).
- [45] A. P. M. Place, L. V. H. Rodgers, P. Mundada, B. M. Smitham, M. Fitzpatrick, Z. Leng, A. Premkumar, J. Bryon, A. Vrajitoarea, S. Sussman, G. Cheng, T. Madhavan, H. K. Babla, X. H. Le, Y. Gang, B. Jäck, A. Geynis, N. Yao, R. J. Cava, N. P. de Leon, and A. A. Houck, New material platform for superconducting transmon qubits with coherence times exceeding 0.3 milliseconds, *Nature Communications* **12**, 1779 (2021).
- [46] A. Potts, G. Parker, J. Baumberg, and P. de Groot, CMOS compatible fabrication methods for submicron josephson junction qubits, *IEEE Proceedings - Science, Measurement and Technology* **148**, 225 (2001).
- [47] M. S. Blok, V. V. Ramasesh, T. Schuster, K. O'Brien, J. M. Kreikebaum, D. Dahlen, A. Morvan, B. Yoshida, N. Y. Yao, and I. Siddiqi, Quantum information scrambling on a superconducting qutrit processor, *Physical Review X* **11**, 021010 (2021).

SUPPLEMENTAL MATERIALS

Laser-Annealing Automation

Automation of laser-annealing is based on JJ image recognition and auto-focusing. For a wafer of 3000 JJs spaced on a grid, we record the coordinates of 10 JJs and perform an affine coordinate transformation to obtain the coordinates of the other JJs. Each JJ is auto-focused by evaluating the image sharpness, which is calculated using the pixel width of macroscopic features such as the Al electrode arms. Afterwards, the JJ is centered to the laser using cross detection of Canny edges of the junction image. The centered, focused JJ is laser-annealed with the input parameters. Images of the JJs are captured for post-processing to exclude those that are improperly focused or centered. This process is also automated using an image structural similarity function that compares any given image with the image of a properly laser-annealed JJ. Images with a structural similarity index less than 0.97 correspond to poorly annealed JJs, and are hence excluded from the data set.

Device Parameters and Fabrication

Microwave properties (eigenmode, linewidth, coupling) of the bus, ROs, and qubits are simulated using Ansys HFSS. For the device shown in Fig. 1(b), qubit-resonator coupling g is 50 MHz and the resonator line-width κ is between 50 and 200 kHz. For the device used for TLS spectroscopy, g is 80 MHz and the κ is 2.5 MHz.

The devices are fabricated on a Si substrate of resistivity $> 10 \text{ k}\Omega$. After surface cleaning of the Si using piranha and buffered-oxide etch (B.O.E.), a 200 nm layer of Nb is sputtered, on which the bus, ROs, and qubit capacitors are defined by electron-beam lithography and reactive ion etching. After an additional B.O.E. cleaning, Al/Al-O_x/Al JJs with nominal critical current densities of $500 \text{ nA } \mu\text{m}^{-2}$ are evaporated in the Manhattan style to form the transmon qubit. Galvanic contact between the Nb capacitor and the JJ is done by a bandaid process [46]. The diced device chips are cleaned using N-Methylpyrrolidone and then wirebonded to a copper cryopackage. A detailed process is given in Ref. [47]. For the JJ test wafers, we remove the piranha cleaning and Nb deposition steps. These test wafers undergo a single deposition step of Al. Thus the JJs are shunted to large Al paddles which are used for resistance probing. A detailed process is given in Ref. [16].

TLS Spectroscopy Cooldown Variations

We calibrate the AC Stark shift by measuring the detuned frequency using a Ramsey sequence at each Stark tone amplitude. The Stark shift follows the frequency shift of an off-resonant Rabi drive in the driving frame: $\sqrt{\Omega^2 + \Delta^2}$, where Ω is the drive amplitude and Δ is the detuning of the drive. Using $\Delta = \pm 80 \text{ MHz}$, we fit our calibration to the function: $\pm(\sqrt{(A\Omega')^2 + \Delta^2} - \Delta)$, where A is a fitted conversion parameter for the drive amplitude Ω' . The calibration of the Stark shift before laser-annealing the transmon is shown in Fig. S1(a). $A = 432 \text{ MHz}$ for $\Delta = -80 \text{ MHz}$ and $A = 416 \text{ MHz}$ for $\Delta = +80 \text{ MHz}$. We calibrate each time before conducting TLS spectroscopy. Here, we measure $P_{|1\rangle}$ at $40 \mu\text{s}$ which is around the T_1 of this transmon. The thermal cyclings of Fig. 3(a) are shown in Figs. S1(b) and (c). The TLS spectroscopy was performed in the following order: Figs. S1(b), Figs. S1(c), and then Fig. 3(a). The consistent TLS mentioned above is seen across all three thermal cycles, with a frequency fluctuation of less than 1 MHz.

We calibrate the Stark shift after laser-annealing the transmon. $A = 459 \text{ MHz}$ for $\Delta = -80 \text{ MHz}$ and $A = 416 \text{ MHz}$ for $\Delta = +80 \text{ MHz}$, shown in Fig. S1(d). We measure $P_{|1\rangle}$ at $80 \mu\text{s}$ which is around the T_1 after laser-annealing. The thermal cyclings of Fig. 3(b) are shown in Figs. S1(e) and (f). The TLS spectroscopy after laser-annealing was performed in the following order: Fig. 3(b), Figs. S1(e), and then Figs. S1(f). No persistent TLS features are seen across all three thermal cycles. For Fig. S1(e), the horizontal orange lines at 50 and 60 hours are acquisition errors since $P_{|1\rangle} = 1$ at all frequencies. We observe telegraphic TLS described in Ref. [26] in Fig. S1(f) at $+20 \text{ MHz}$ from 0 to 10 hours.

Wafer Scale Characterization

For the COMSOL simulation, we utilize a *Heat Transfer in Solids* model with convection cooling and a Gaussian beam heat source to thermally simulate laser-annealing. 37.4% of power reflected by silicon is taken into account.

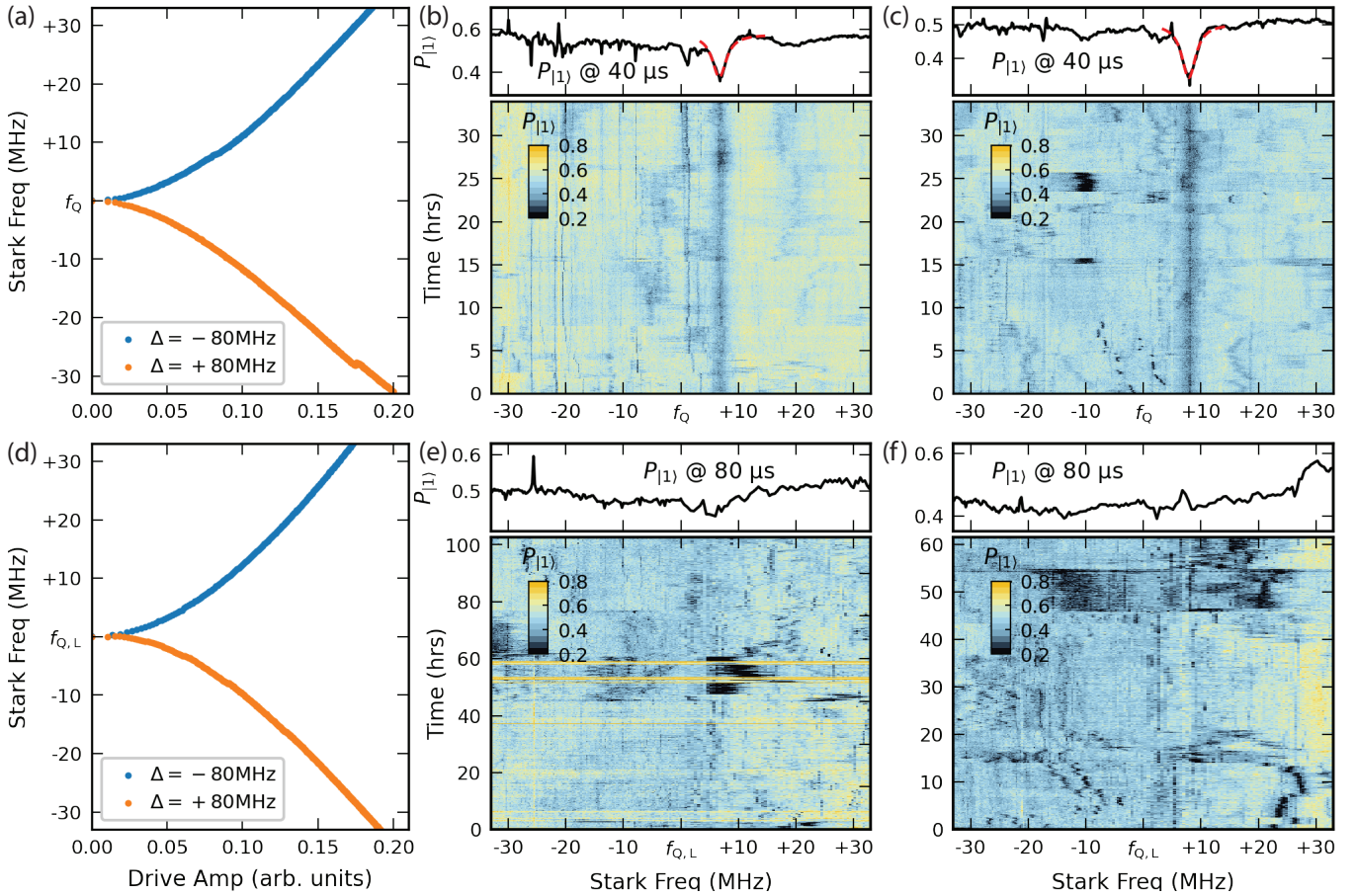


FIG. S1. (a) Calibration of AC Stark shift of transmon before laser-annealing. $\Delta = \pm 80$ MHz refers to Stark tone positively/negatively detuned from qubit: $f_{\text{stark}} = f_Q \pm 80$ MHz. (b) TLS spectroscopy after thermal cycling of Fig. 3(b). The TLS feature lies at $f_{\text{TLS}} = f_Q + 6.68$ MHz. (c) TLS spectroscopy after second thermal cycling. $f_{\text{TLS}} = f_Q + 7.89$ MHz. (d) Calibration after laser-annealing. (e) TLS spectroscopy after thermal cycling of Fig. 3(c). No persistent TLS features are seen. (f) TLS spectroscopy after second thermal cycling.

Convection cooling with room temperature of 20°C is input into the simulation. The beam is centered on the junction of interest, while another junction is placed 1.2 mm away to observe the temperature of neighboring junctions. The simulated temperature of the neighboring junction is 22.9°C . We fit the simulated temperature to the resistance data given in Fig. 4(a) using the function: $\Delta R/R_0 = m - b \exp(-T/T_0)$, where m is the final resistance change, b determines the initial resistance, and T_0 is the characteristic temperature (red dashed line of Fig. 4(a)).

The lasing parameters for each wafer-scale study are described in Table. S1. For each study, we vary a single parameter and keep all other parameters fixed. The normalized resistance change $\Delta R/R_0$ with respect to exposure time and repetition are shown in Figs. S2(a) and (b). Both exhibit an exponentially plateauing increase, similar to Fig. 4(a). This suggests that the total amount of heat deposited on the JJ, which is a function of lasing power, exposure time, and exposure repetition, determines the increase in resistance. Each datapoint shown in Figs. 4 and Fig. S2 exhibits uncertainty $\sim 1\%$. This implies identically laser-annealed JJs will vary in resistance change. Therefore for precise tuning of R_N , JJs need to be iteratively annealed while R_N is monitored. This will require multiple resistance probings of the qubit capacitor pads. The effects of this on qubit frequency and quality should be investigated.

In Fig. S2, the calculated absorption with respect to displacement (blue dashed line) as well as $H(D)$ (black dashed line) used for fitting Fig. 4(b) are shown. The absorption plateaus until $D = 4 \mu\text{m}$, which corresponds to the displacement in which the beam moves away from the Al and onto the Si as mentioned in the main text. Due to this plateau, a kink arises when the absorption is multiplied with $H(D)$, as shown by the red line (equal to the fit shown in Fig. 4(b), but scaled down for clarity). Further analysis of the thermal conduction to the JJ ($H(D)$) with respect to beam displacement is needed.

Study	Power	Displacement	Exposure Time	Exposure Repetition	Aging (Wafer1)	Aging (Wafer2)
Applied Power	Varied	40 mW	40 mW	40 mW	40 mW	40 mW
Applied Displacement	0 μm	Varied	0 μm	0 μm	0 μm	0 μm
Applied Exposure Time	60 s	60 s	Varied	60 s	60 s	60 s
Applied Exposure Repetition	1	1	1	Varied	1	1
Utilized Wafer Age	69 d	88 d	75 d	71 d	0 d to 30 d	135 d to 170 d

TABLE S1. Lasing parameters for each wafer-scale study.

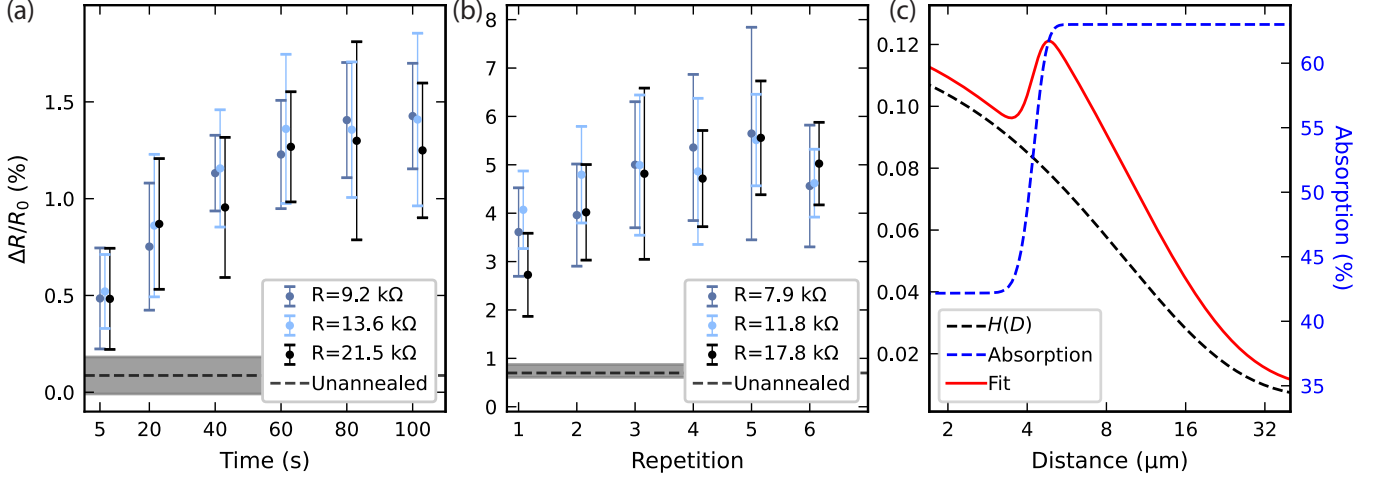


FIG. S2. (a) Percent JJ resistance change vs laser exposure time. (b) Percent JJ resistance change vs exposure repetition. (c) Calculated absorption and $H(D)$ used to produce the fit given in Fig. 4(b). The product is shown by the solid red line, which is identical to that shown in Fig. 4(b) but scaled down for clarity.

Microscopic Imaging

In order to correlate barrier thickness to resistance, we measure the surface area and barrier thickness of unannealed, laser-annealed, and thermally annealed JJs using scanning electron microscopy (SEM) and high resolution transmission electron microscopy (HRTEM). The SEM is a Zeiss Gemini Ultra SEM and the HRTEM is performed using the Transmission Electron Aberration-corrected Microscope 1 (TEAM1) at the National Center for Electron Microscopy (NCEM). The TEAM1 has a resolution of 0.1 nm. For barrier thickness measurements, we utilize electron energy loss spectroscopy (EELS) using a Gatan Tridiem EELS spectrometer on the HRTEM results. The EELS measurements provide the JJ barrier thickness dispersion discussed in the main text. We utilize JJs on a 1x1 cm² diced section of our JJ test wafers. The SEM and HRTEM images are shown in Fig. S3. The measured R_N , area, and barrier thickness are given in Table. S2.

We fit the area-normalized R_N to $\exp(t/\tau)$, where t is the measured barrier thickness and τ is the characteristic barrier thickness. We obtain $\tau = 0.39 \pm 0.23$ nm, which implies an increase of 1 \AA in t will increase R_N by $\sim 30\%$ as stated in the main text. However, the fit is limited due to the lack of statistics and large dispersion. This dispersion is due to the curvature of the tunneling barrier in our HRTEMs. Additional statistics are needed to properly correlate JJ barrier thickness to R_N .

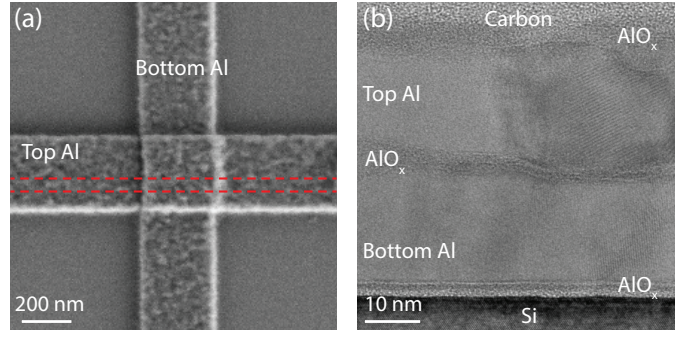


FIG. S3. (a) Scanning electron microscopy (SEM) of laser-annealed JJ. The red dash corresponds to the area on which a focused ion beam (FIB) is applied to acquire the cross-section of the JJ for high resolution transmission electron microscopy (HRTEM). (b) HRTEM of JJ shown in (a). Each layer is given a corresponding label. The top layer of carbon is due to the FIB process. SEM and HRTEM images for the other four JJs given in Table. S2 appear similar to that given here.

Sample	Resistance	Area	Barrier Thickness
Unannealed	7781 Ω	0.0997 μm^2	2.43 \pm 0.71 nm
Unannealed	5249 Ω	0.1679 μm^2	2.32 \pm 0.39 nm
Laser-Annealed	5979 Ω	0.1125 μm^2	2.44 \pm 0.54 nm
400 $^\circ\text{C}$ -Annealed	13 735 Ω	0.1967 μm^2	2.44 \pm 0.23 nm
400 $^\circ\text{C}$ -Annealed	13 867 Ω	0.1835 μm^2	2.64 \pm 0.07 nm

TABLE S2. Measured resistance, area, and barrier thickness of five JJs. Two are unannealed, one is laser-annealed, and two are thermally annealed at 400 $^\circ\text{C}$.